AMERICAN JOURNAL OF PHYSIOLOGY
RENAL PHYSIOLOGY

Am J Physiol Renal Physiol 323: F577–F589, 2022.
First published August 26, 2022; doi:10.1152/ajprenal.00156.2022

RESEARCH ARTICLE

Metabolomic profiling reveals muscle metabolic changes following iliac arteriovenous fistula creation in mice

Ram B. Khattri,[1]* Kyoungrae Kim,[1]* Erik M. Anderson,[2,4] Brian Fazzone,[2,4] Kenneth C. Harland,[2,4] Qiongyao Hu,[2,4] Victoria R. Palzkill,[1] Tomas A. Cort,[1] Kerri A. O'Malley,[2,4] Scott A. Berceli,[2,4] Salvatore T. Scali,[2,4] and Terence E. Ryan[1,3]

[1]Department of Applied Physiology and Kinesiology, University of Florida, Gainesville, Florida; [2]Division of Vascular Surgery and Endovascular Therapy, University of Florida, Gainesville, Florida; [3]Center for Exercise Science, University of Florida, Gainesville, Florida; and [4]Malcom Randall Veterans Affairs Medical Center, Gainesville, Florida

Abstract

End-stage kidney disease, the most advanced stage of chronic kidney disease (CKD), requires renal replacement therapy or kidney transplant to sustain life. To accomplish durable dialysis access, the creation of an arteriovenous fistula (AVF) has emerged as a preferred approach. Unfortunately, a significant proportion of patients that receive an AVF experience some form of hand dysfunction; however, the mechanisms underlying these side effects are not understood. In this study, we used nuclear magnetic resonance spectroscopy to investigate the muscle metabolome following iliac AVF placement in mice with CKD. To induce CKD, C57BL6J mice were fed an adenine-supplemented diet for 3 wk and then randomized to receive AVF or sham surgery. Two weeks following surgery, the quadriceps muscles were rapidly dissected and snap frozen for metabolite extraction and subsequent nuclear magnetic resonance analysis. Principal component analysis demonstrated clear separation between groups, confirming a unique metabolome in mice that received an AVF. AVF creation resulted in reduced levels of creatine, ATP, and AMP as well as increased levels of IMP and several tricarboxylic acid cycle metabolites suggesting profound energetic stress. Pearson correlation and multiple linear regression analyses identified several metabolites that were strongly linked to measures of limb function (grip strength, gait speed, and mitochondrial respiration). In summary, AVF creation generates a unique metabolome profile in the distal skeletal muscle indicative of an energetic crisis and myosteatosis.

NEW & NOTEWORTHY Creation of an arteriovenous fistula (AVF) is the preferred approach for dialysis access, but some patients experience hand dysfunction after AVF creation. In this study, we provide a detailed metabolomic analysis of the limb muscle in a murine model of AVF. AVF creation resulted in metabolite changes associated with an energetic crisis and myosteatosis that associated with limb function.

chronic kidney disease; dialysis; renal; skeletal muscle

INTRODUCTION

Chronic kidney disease (CKD) is caused by a progressive loss of kidney function resulting in the inability of the kidney to properly filter waste products from the blood. End-stage kidney disease (ESKD), the most advanced stage of CKD, occurs when kidney function cannot meet the body's demands (1, 2). Unfortunately, there are no pharmacological treatments for ESKD, and these patients require either renal replacement therapies (hemodialysis or peritoneal dialysis) or kidney transplant to sustain life. Obtaining durable vascular access is a major challenge that impedes the expansion of dialysis treatment in patients with ESKD. The creation of an arteriovenous fistula (AVF), compared with arteriovenous grafts and tunneled dialysis catheter placement, has become the preferred approach to provide functional hemoaccess because of improved patency and morbidity/mortality rates. Unfortunately, many patients with ESRD experience a spectrum of access-related hand dysfunction (ARHD) after AVF creation, ranging from mild sensory or motor impairments to complete monoparesis and, in severe cases, digital gangrene (3). The underlying mechanisms associated with ARHD are not fully understood, but historically the severity of ARHD has been largely attributed to hemodynamic changes following AVF creation. However, recent work has demonstrated that hemodynamic changes alone do not explain the symptomatology of ARHD (3), suggesting that other factors, such as neuromuscular health, may contribute to ARHD.

The presence of sensory and motor impairment in patients with ARHD suggest that at least some of the pathophysiology involves alterations in the neuromuscular system

---

*R. B. Khattri and K. Kim contributed equally to this work.

Correspondence: S. T. Scali (Salvatore.Scali@surgery.ufl.edu); T. E. Ryan (ryant@ufl.edu).

Submitted 8 June 2022 / Revised 22 August 2022 / Accepted 22 August 2022

(i.e., motor neurons and skeletal myofibers). To this end, both the CKD milieu (uremic toxins, metabolic acidosis, and inflammation) and hemodynamic changes (decreased limb perfusion) have been shown to independently (4–7) and additively impact neuromuscular health/function (8). Central to these changes are disturbances in muscle metabolism, which have been suggested to exert critical influence on the neuromuscular system (9–12). However, the impact of AVF creation on the neuromuscular system in the hand/forearm has not been meticulously interrogated.

Progress toward understanding the clinical and physiological domains responsible for ARHD has been hindered by the lack of a suitable preclinical model that replicates the clinical spectrum of hand pathology. Current murine AVF models have been focused on the biology of AVF maturation and vessel remodeling but exclusively use either the carotid artery/jugular vein or the distal aorta/inferior vena cava (13–17). Unfortunately, these models are unable to recapitulate the pathophysiology of ARHD due to their anatomic locations. Recently, our group developed a new mouse iliac AVF model to address this issue (18). Creation of a fistula between the iliac artery and vein produces clinically relevant changes in the surgical hindlimb, including hemodynamic alterations, muscle weakness, and mitochondrial function impairment. In the present study, we hypothesized that the creation of an iliac AVF would result in significant alterations to the limb muscle metabolome.

METHODS

Chemicals

Chemicals used to prepare samples for metabolomics included sodium mono-and-dibasic sodium phosphate, EDTA, sodium azide (NaN_3), deuterated chloroform ($CDCl_3$), and deuterated water and were purchased from either Millipore-Sigma (St. Louis, MO) or Cambridge Isotope Laboratories (Andover, MA). D_6-4,4-dimethyl-4-silapentane-1-sulfonic acid (D_6-DSS) was procured from FUJIFILM Wako (Richmond, VA). Detailed information about other chemicals can be found in our previous study (19).

Animal Use and Models

A total of 36 C57BL/6J male mice (~8 wk old) were obtained from Jackson Laboratory (Stock No. 000664). These animals were housed with 5 mice/cage in a temperature (22°C)-controlled room with a 12:12-h light-dark cycles. We used an adenine diet model to induce CKD as previously described (5, 7, 8). Briefly, mice were acclimated to a standard casein-based chow (control diet) for 7 days. Thereafter, animals were randomly assigned to either remain on the control diet (non-CKD groups) or receive an adenine-supplemented diet to induce CKD. Following 3 wk of the casein/adenine diet, animals were randomly assigned to receive either AVF surgery or sham surgery (Fig. 1A). Detailed descriptions of the iliac AVF surgery and postoperative care can be found in our previous study (18). Briefly, mice were anesthetized using inhaled isoflurane (2–3% induction and 1–1.5% maintenance), and creation of the iliac AVF was accomplished using longitudinal venotomy followed by an elliptical incision to remove the common walls of the iliac artery and vein, creating an ~0.8- to 0.9-mm AVF. The venotomy was closed with 10-0 sutures, and heparin (0.2 IU/g body wt) was administered. Sham surgeries involved completed dissection and vessel clamping but without a venotomy or AVF creation. Mice were treated for analgesia using buprenorphine (0.1 mg/kg body wt) and 0.9% saline for a postoperative period of 48 h. These experiments were carried out following the guidelines provided in the National Institutes of Health Guide for the Care and Use of Laboratory Animals and any updates. All procedures were approved by the Institutional Animal Care and Use Committees of the University of Florida and Malcom Randall Veterans Affairs Medical Center.

Assessment of Renal Function

Renal function was assessed by quantification of blood urea nitrogen using a commercially available colorimetric assay kit (K024, Arbor Assays). Glomerular filtration rate was also measured in live animals using fluorescein isothiocyanate-labeled inulin clearance as previously described (6, 18, 20, 21).

Limb Perfusion

Laser-Doppler flowmetry (moorVMS-LDF, Moor Instruments) was used to monitor perfusion rates in the tibialis anterior (TA) muscle and paw as previously described (8, 18).

Assessment of Hindlimb Function

Unilateral hindlimb grip strength was measured by allowing mice to grasp a T-bar attached to a Bio-GS3 grip strength meter (BIOSEB). Once firmly grasping the T-bar, the mouse was gently pulled away and maximal strength was measured. A total of five trials were performed, and the highest value was normalized to the contralateral limb (expressed as a percentage) and used for analysis. Gait speed was measured using a DigiGait treadmill system by gradually increasing belt speed up to 20 cm/s. The highest tolerable speed was recorded for each mouse.

Tissue Harvest

Two weeks after surgery, mice were anesthetized using isoflurane and the left quadriceps muscle was rapidly dissected and immediately frozen in liquid nitrogen. Samples were stored at −80°C until the time of metabolite extraction.

Skeletal Muscle Histology

The TA muscle was frozen in optimal cutting temperature compound (OCT) compound using liquid nitrogen-cooled isopentane and cryosectioned using a Leica 3050S. Ten-micrometer transverse sections were mounted to microscope slides. Myofiber cross-sectional area (CSA) was analyzed using anti-laminin antibody (L9393, Millipore-Sigma, 1:100 dilution) incubated overnight at 4°C. Following washes with PBS, sections were then incubated with secondary antibody (Alexa Fluor 488 goat anti-rabbit IgG, 1:250 dilution) and biotinylated *Griffonia simplicifolia* lectin I (GSL I) isolectin B4 (Vector Laboratories, Dylight 649 conjugate, 1:200 dilution) for 1 h at room temperature. Coverslips were mounted using a medium containing DAPI to label nuclei (H-1500, Vector Laboratories). Images were collected using a ×20 objective on an Evos FL2

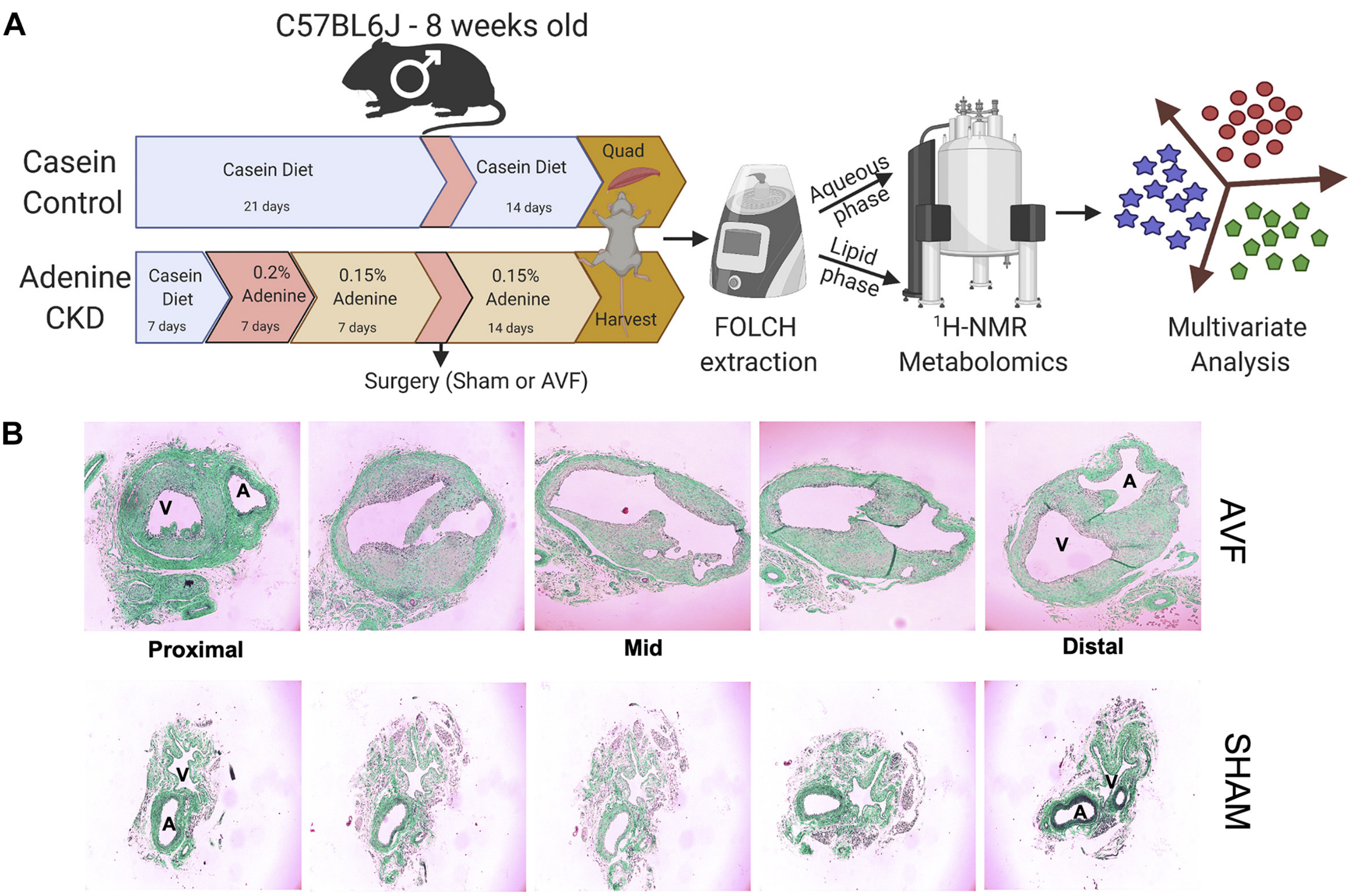

Figure 1. *A*: schematic description of the experimental design. Animals were exposed to either casein or adenine diet for 3 wk and randomly allocated to receive arteriovenous fistula (AVF) or sham surgery. Following 2 wk of recovery, quadriceps muscle tissues were taken and underwent metabolite extraction, nuclear magnetic resonance (NMR) processing, and data analysis. *B*: representative Masson's trichrome-stained cross sections of left common iliac arteriovenous for AVF (*top*) and sham (*bottom*) from the proximal to distal site. The proximal and distal images shown are 0.5 mm on either side of the anastomosis. The three *middle* images shown within the AVF are separated by 0.4 mm. The total length of the anastomosis created in this model is 0.8–0.9 mm. A, artery; CKD, chronic kidney disease; V, venous.

Auto microscope (Thermo Fisher Scientific). Tiled images of the entire muscle section were used for automated analysis myofiber CSA and capillary numbers using MuscleJ (22). Centrally nucleated myofibers were analyzed manually using ImageJ. Masson trichrome staining (HT15, Millipore-Sigma) was used to assess muscle fibrosis. Quantification of the fibrotic area was performed in ImageJ using an automated threshold selection (hue: 140/196, saturation: 0/255, brightness: 110/255) and expressed as a percentage of the total image area. All image analysis was performed using coded images and blinding of investigators to the grouping of animals.

Assessment of Mitochondrial Respiratory Function

Mitochondria were isolated from surgical gastrocnemius and plantaris muscles, and assessment of mitochondrial bioenergetics was performed as previously described (18, 19). Mitochondrial respiratory function was analyzed using a creatine kinase clamp system, which we have previously described in detail (7, 19, 20). Mitochondria were fueled with pyruvate (5 mM), malate (2.5 mM), and octanoylcarnitine (0.2 mM), and rates of respiration were assessed at physiologically relevant levels of energy demand controlled by the creatine kinase clamp system.

Metabolite Extraction

Weights of frozen quadriceps specimens were weighed using a microbalance (Mettler-Toledo, Columbus, OH). Next, a slightly modified FOLCH (23) extraction was performed to extract aqueous- and lipid phase metabolites. Details of the extraction protocol can be found in our previous publications (5, 24). The aqueous phase was lyophilized overnight (Labconco, Kansas, MO), and the lipid phase was dried with inert nitrogen gas. The resulting aqueous and lipid phase dry powders were stored at −80°C until analysis using nuclear magnetic resonance (NMR).

NMR-Based Metabolomics

The dry powder of aqueous phase samples was dissolved in 50 μL of phosphate buffer system (50 mM, pH 7.2) consisting of 0.5 mM D$_6$-DSS, 2 mM EDTA, and 0.2% NaN$_3$. Lipid phase dry powders were dissolved in 70 μL of CDCl$_3$ supplemented with 10 mM pyrazine (as an internal NMR standard). All samples were loaded into 1.5-mm optical density NMR tubes. An 800 MHz/54 mm Bruker Avance III system (Bruker BioSpin, Billerica, MA) with a 5-mm TCl CryoProbe was used to acquire all one-dimensional (1-D) and two-dimensional

(2-D) NMR spectra. 1-D ^{1}H spectra were acquired with the first slice of 1-D nuclear Overhauser effect spectroscopy (NOESY) pulse sequence (noesypr1d) (25), using previously described parameters (5, 24). 2-D spectra including heteronuclear single quantum coherence, heteronuclear multiple bond coherence, correlated spectroscopy, and total correlated spectroscopy were acquired using the standard Bruker library as well as previous work (26) to confirm metabolite identity. All spectra were acquired at room temperature.

NMR Data Processing and Analysis

MestReNova (14.1.2-25024) software (Mestrelab Research, Santago de Compostela, Spain) was used to process all NMR spectra. For 1-D NOESY spectra, line broadening of 0.22 Hz and 64,000 data points zero filling were applied before Fourier transformation. Before peak integral areas were extracted for quantitative purpose, 1-D spectra were phase and baseline (spline method) corrected, referenced, and normalized. All aqueous phase spectra were referenced and normalized with the D$_6$-DSS internal NMR reference at 0.00 ppm. For lipid phase spectra, the CDCl$_3$ peak at 7.26 ppm was used to reference all peaks and the pyrazine peak (at 8.61 ppm) was used for normalization. Muscle weight was further used to normalize peak integral areas or concentration values for all metabolites. For peaks with overlap, Chenomx Suite 8.6 NMR software (Chenomx, Edmonton, AB, Canada) was used to determine concentrations. Previously published work (5, 24, 27, 28), Chenomx Suite 8.6 NMR software, the biological magnetic resonance bank (29), and a set of 2-D spectra were used to assign and verify metabolite identity (see Supplemental Figs. S4, S5, S6, and S7).

Statistical Analysis

Principal component analysis (PCA) and partial-least square discriminant analysis (PLS-DA) were performed using the web-based platform Metaboanalyst 5.0 (https://www.metaboanalyst.ca/). Within Metaboanalyst 5.0, NMR noise was excluded from false discovery rate corrected data by applying interquartile range filtering. Furthermore, probability quotient normalization along with pareto/auto scaling were applied. PLS-DA was validated with a Q^2 test. PLS-DA-based variable importance in projection (VIP) plots were used to determine the significance of metabolites/compounds among the groups, with VIP scores of ≥ 1 considered as significant. Graphs were generated using GraphPad Prism [v.9.2.0 (332), GraphPad Software, San Diego, CA]. Two-way ANOVA with Tukey's multiple comparisons tests were performed with $P \leq 0.05$ considered significant. Data are presented as means ± SD or as box and whisker plots with 95% confidence intervals. Pearson correlation coefficients between metabolite abundance and functional outcomes were performed in SPSS software (version 27) with a two-tailed $P \leq 0.05$ considered significant following correction for multiple comparisons using Benjamini and Hochberg false discovery rate. To determine the metabolites associated with functional outcome (grip strength, gait speed, and mitochondrial respiratory capacity), we performed stepwise multiple linear regression analyses using SPSS software (v.27). Metabolites included in these analyses were selected based on two levels of evidence: *1*) a significant correlation with functional outcomes and *2*) a significant effect of either CKD or AVF. Metabolites that did not meet these two criteria were excluded from the multiple regression analysis. For metabolites included, regression was performed using data from both sham and AVF mice. To validate the models, the assumption of multicollinearity was assessed by the variance inflation factor and the normality of residual distribution was checked by visible inspection of histograms.

RESULTS

Source data for this study can be found here: https://doi.org/10.6084/m9.figshare.20000147.v2. Supplemental figures and tables can be accessed at the following link: https://doi.org/10.6084/m9.figshare.20000153.v2.

Table 1. *Characteristics of animals and effect of AVF creation on limb function*

Treatment Group	Control (n = 5)	Control (n = 8)	CKD (n = 5)	CKD (n = 10)
Surgery	Sham	AVF	Sham	AVF
Body mass, g	28.4 ± 1.1	26.4 ± 2.1	23.6 ± 2.1*	24.7 ± 1.3
Quad mass, mg	200 ± 41.0	168.3 ± 31.5	175.0 ± 24.7	192.4 ± 36.2
Kidney function				
Glomerular filtration rate, µL/min	435.6 ± 58.6	362.8 ± 89.5	117.4 ± 65.2*†	163.6 ± 113.9*†
Blood urea nitrogen, mg/dL	20.8 ± 4.6	22.1 ± 2.4	41.2 ± 6.3*†	39.4 ± 9.2*†
Hemodynamics				
TA, % contralateral leg	93.6 ± 4.4	62.7 ± 12.7*‡	101.6 ± 3.2	57.0 ± 27.3*‡
Paw, % contralateral leg	98.0 ± 2.5	64.3 ± 18.6*‡	102.7 ± 1.6	42.7 ± 19.5*‡
Hindlimb function				
Gait speed, cm/s	20.0 ± 0.0	16.5 ± 5.0	20.0 ± 0.0	14.3 ± 5.2*‡
Grip strength, % contralateral leg	111.5 ± 8.6	66.1 ± 36.2*	93.3 ± 11.0	41.4 ± 35.1*‡
Mitochondrial function				
Respiratory capacity, pmol/s/mg	12,870 ± 1,203	5,407 ± 3,582*	8,443 ± 1,509*	4,478 ± 3,685*‡
OXPHOS conductance	1,042 ± 97	411 ± 296*	693 ± 127*	356 ± 294*
Muscle histopathology (TA)				
Cross-sectional area, µm^2	2,550 ± 449	1,818 ± 741	1,979 ± 182	1,643 ± 310
Capillary contacts per fiber	5.8 ± 1.6	4.0 ± 2.2	5.8 ± 0.4	3.4 ± 2.1
Fibrosis, %	1.8 ± 0.5	7.8 ± 4.5	2.0 ± 0.6	13.5 ± 12.8*‡

Kidney function was measured prior to surgery, blood perfusion at *postoperative day 3*, gait speed at *postoperative day 4*; and grip strength at *postoperative day 4*. AVF, arteriovenous fistula; CKD, chronic kidney disease; TA, tibialis anterior. *$P < 0.05$ vs. control sham; †$P < 0.05$ vs. control arteriovenous fistula (AVF); ‡$P < 0.05$ vs. chronic kidney disease (CKD) sham.

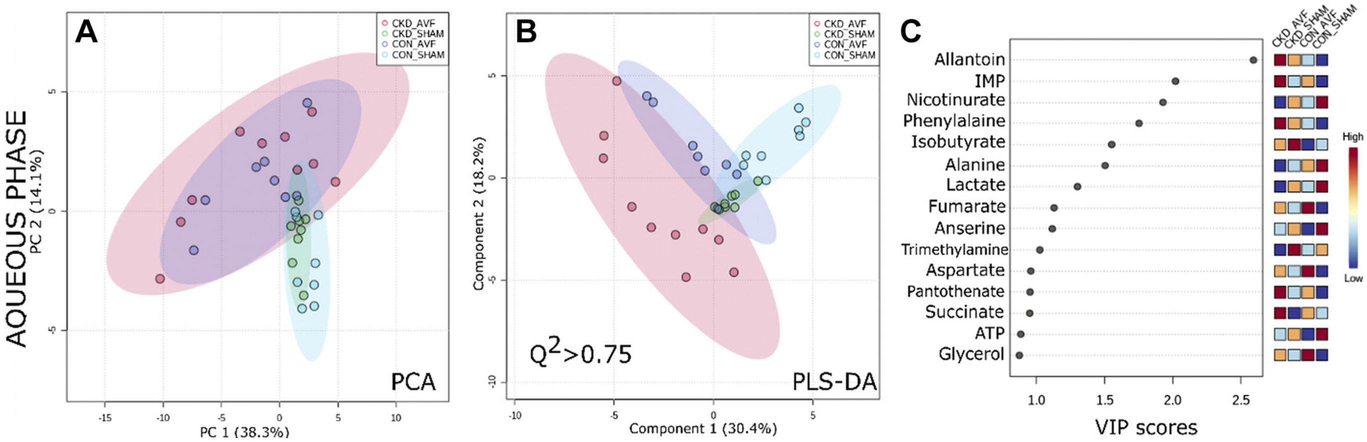

Figure 2. Statistical analysis of water-soluble metabolites in chronic kidney disease (CKD) arteriovenous fistula (AVF) (*n* = 10), CKD sham (*n* = 10), control (CON) AVF (*n* = 8), and CON sham (*n* = 7) quadriceps samples determined with Metaboanalyst 5.0 (web-based tools). Principal component analysis (PCA; *A*), partial least squares discriminant analysis (PLS-DA) with Q^2 value (*B*), and variable importance in projection (VIP) scores (*C*) obtained from ^{1}H nuclear magnetic resonance data.

Impact of CKD and AVF Creation

To explore the impact of CKD and AVF creation on the muscle metabolome, we used the study design shown in Fig. 1*A*. Table 1 shows selected clinical and physical characteristics of the animals used in this study. Figure 1*B* shows representative histological samples of serial sectioned iliac vascular bundles demonstrating clear AVF

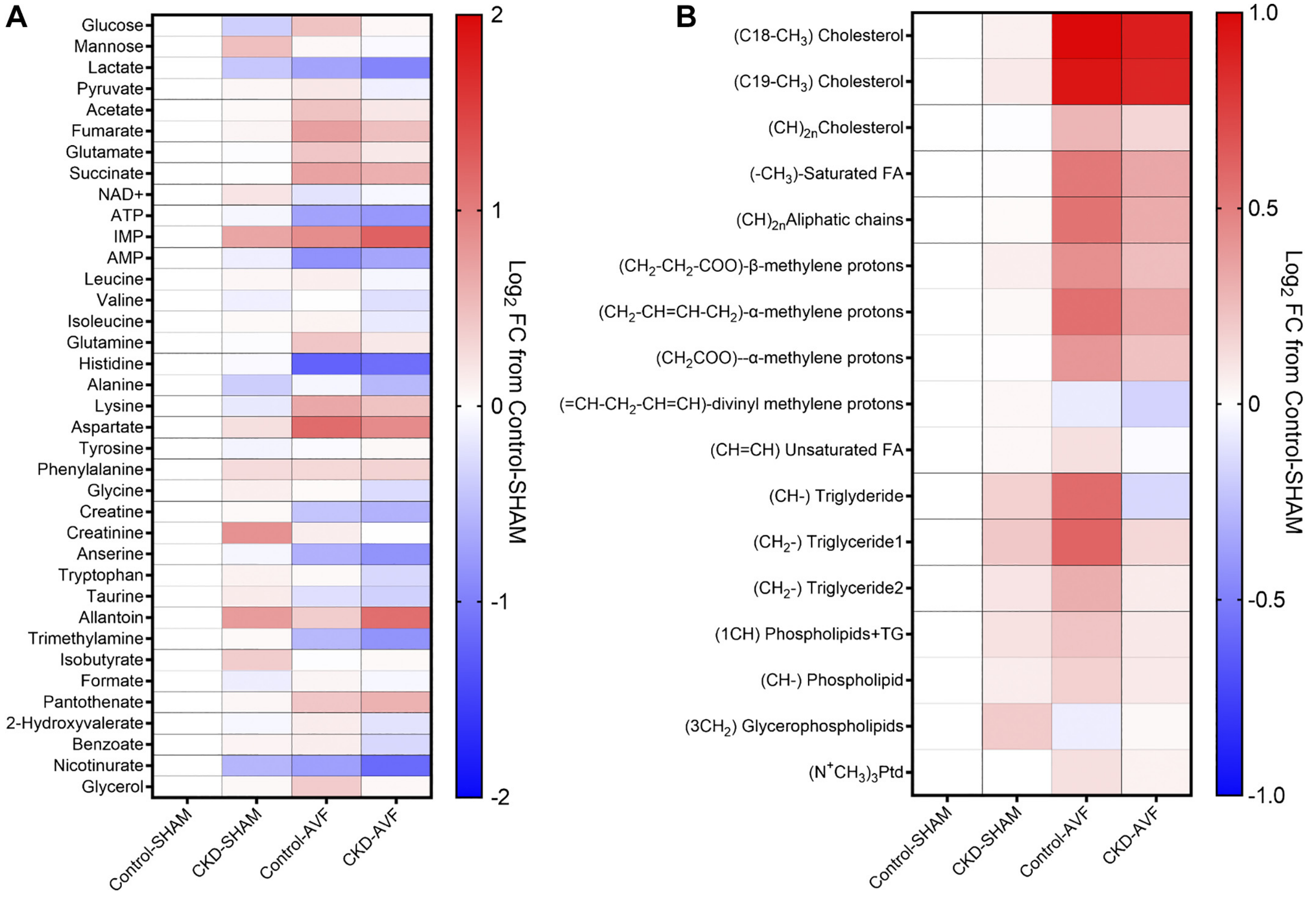

Figure 3. Heatmap illustrating $\log_2$-transformed fold changes (FCs) from the control-sham group of metabolites assessed for the aqueous phase (*A*) and organic phase samples (*B*) (*n* = 7–10/group). AVF, arteriovenous fistula; CKD, chronic kidney disease; FA, fatty acid, NAD + , nicotinamide adenine dinucleotide; Ptd, phosphatidylcholine; TG, triglyceride.

creation. Consistent with previous studies, adenine-fed mice displayed a significant reduction in renal function as evidenced by lower glomerular filtration rates and elevated blood urea nitrogen (5, 30, 31). Laser-Doppler measurements of perfusion demonstrated mild hemodynamic alterations in the TA muscle and dorsal paw following AVF creation (Fig. 1*B*). Consequently, gait speed (walking performance) and hindlimb grip strength were significantly lower in AVF groups (Table 1). Examination of muscle mitochondrial function revealed that CKD and AVF both independently reduced performance of oxidative phosphorylation (Table 1). Notably, the impairments in strength/walking performance and muscle metabolism occurred in the absence of significant changes in muscle mass (Table 1).

Multivariate Analysis Identifies Distinct Metabolome Grouping Following AVF Creation

The identified metabolites from both aqueous phase and lipid phase extracts were subjected to PCA and PLS-DA using false discovery rate correction data to reduce dimensionality and investigate intrinsic variation among groups. PCA showed clustering among the four groups with clear separation among the groups that received AVF surgery for both aqueous (Fig. 2*A*) and lipid phase metabolites (Supplemental Fig. S1*A*). Similarly, supervised PLS-DA resulted in a Q^2 value above 0.75 for aqueous phase samples, indicating a higher predictive nature of the model for classifying CKD and AVF groups (Fig. 2*B*). However, lipid phase sample showed a Q^2 value below 0.4 (Supplemental Fig. S1*B*). The VIP score plot (obtained from PLS-DA) identified important metabolites responsible for the differences among the four groups (Fig. 2*C*). For lipid phase metabolites, only cholesterol, triglyceride, and saturated and unsaturated fatty acids showed VIP scores of >1 (Supplemental Fig. S1*C*).

AVF Creation Alters the Muscle Metabolomic Signature

There was a total of 37 metabolites in the aqueous phase samples that were quantifiable across all four groups (Supplemental Table S1). A heatmap showing $\log_2$-transformed fold change (relative to control-sham) metabolite abundances for all aqueous phase metabolites is shown in Fig. 3*A*. For lipid phase extract, 18 peaks were quantifiable across all samples (Supplemental Table S1 and Supplemental Fig. S3). A heatmap showing $\log_2$-transformed fold change (relative to control-sham) metabolite abundances for all organic phase metabolites is shown in Fig. 3*B*. Notably, creation of the AVF, regardless of the presence/absence of CKD, resulted in clear alterations to both aqueous and lipid phase metabolomes.

Next, we used two-way ANOVA to interrogate the independent and interactive effects of CKD and AVF creation on metabolite abundance. CKD, alone, was found to alter the

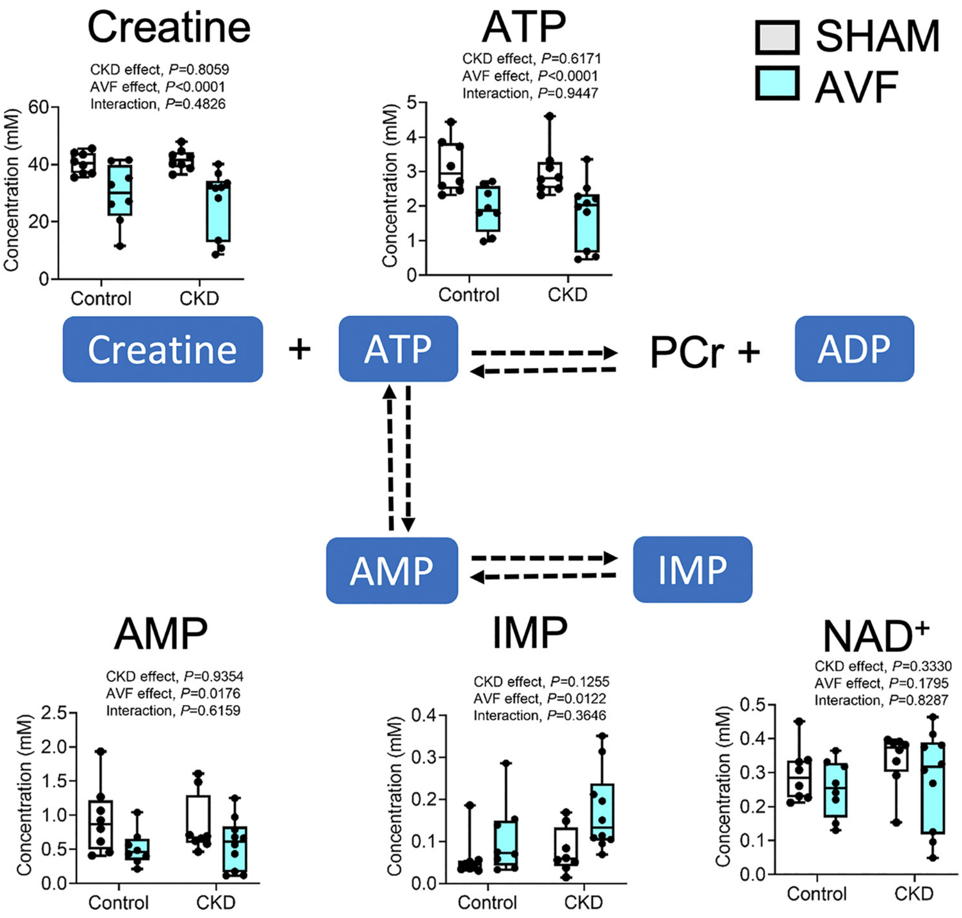

Figure 4. Graphical depiction for energy metabolism in skeletal muscle (quadriceps) with quantified metabolites shown as box and whisker plots (with 95% confidence intervals) in chronic kidney disease (CKD) arteriovenous fistula (AVF) (*n* = 10), CKD sham (*n* = 10), control (CON) AVF (*n* = 8), and CON sham (*n* = 7) groups. The *y*-axis is the concentration (in mM). Statistical analysis was performed using two-way ANOVA. NAD+, nicotinamide adenine dinucleotide.

abundances of several metabolites including valine, lactate, alanine, allantoin (a product of adenine catabolism), and nicotinurate ($P \leq 0.05$). These findings are consistent with a previous study (5). AVF creation significantly altered ~50% of the metabolites detected in both aqueous and lipid phases ($P \leq 0.05$) (Supplemental Table S1). AVF creation decreased the levels of ATP, AMP, and creatine, whereas IMP levels were significantly increased (Fig. 4). These metabolite changes are suggestive of a profound energetic stress, which likely stems from the combined effects of mitochondrial dysfunction, mild ischemia, and the uremic milieu. Mice with AVF also exhibited significantly higher levels of succinate, fumarate, and glutamate compared with sham mice, all metabolites that feed the tricarboxylic acid (TCA) cycle (Fig. 5). Moreover, lactate levels were significantly lower in AVF mice, whereas glucose and pyruvate levels were unaffected by AVF placement (Fig. 5). The accumulation of TCA cycle intermediates coupled with the degree of mitochondrial respiratory impairment (Table 1) suggest that metabolic disturbances arising from AVF creation most likely stem from dysfunction in the enzymes of the mitochondrial electron transport system.

We next explored amino acid levels following surgery. AVF creation increased several amino acids including glutamate, glutamine, lysine, and aspartate (Fig. 6). In contrast, AVF creation significantly decreased the levels of histidine and anserine, which are related to carnosine, a metabolite highly abundant in muscle tissues and known for its antioxidant properties (32, 33). Neither AVF creation nor CKD was found to impact branched-chain amino acid levels (leucine, isoleucine, and valine). AVF creation also increased the levels of succinate and fumarate, findings consistent with models of myocardial ischemia (34, 35). For lipid-soluble compounds, saturated fatty acids and cholesterols were significantly elevated following AVF surgery ($P \leq 0.05$) (Fig. 7 and Supplemental Table S1).

Metabolites Associated With Limb Function

To explore associations between limb function and metabolites changes induced by AVF placement, we calculated

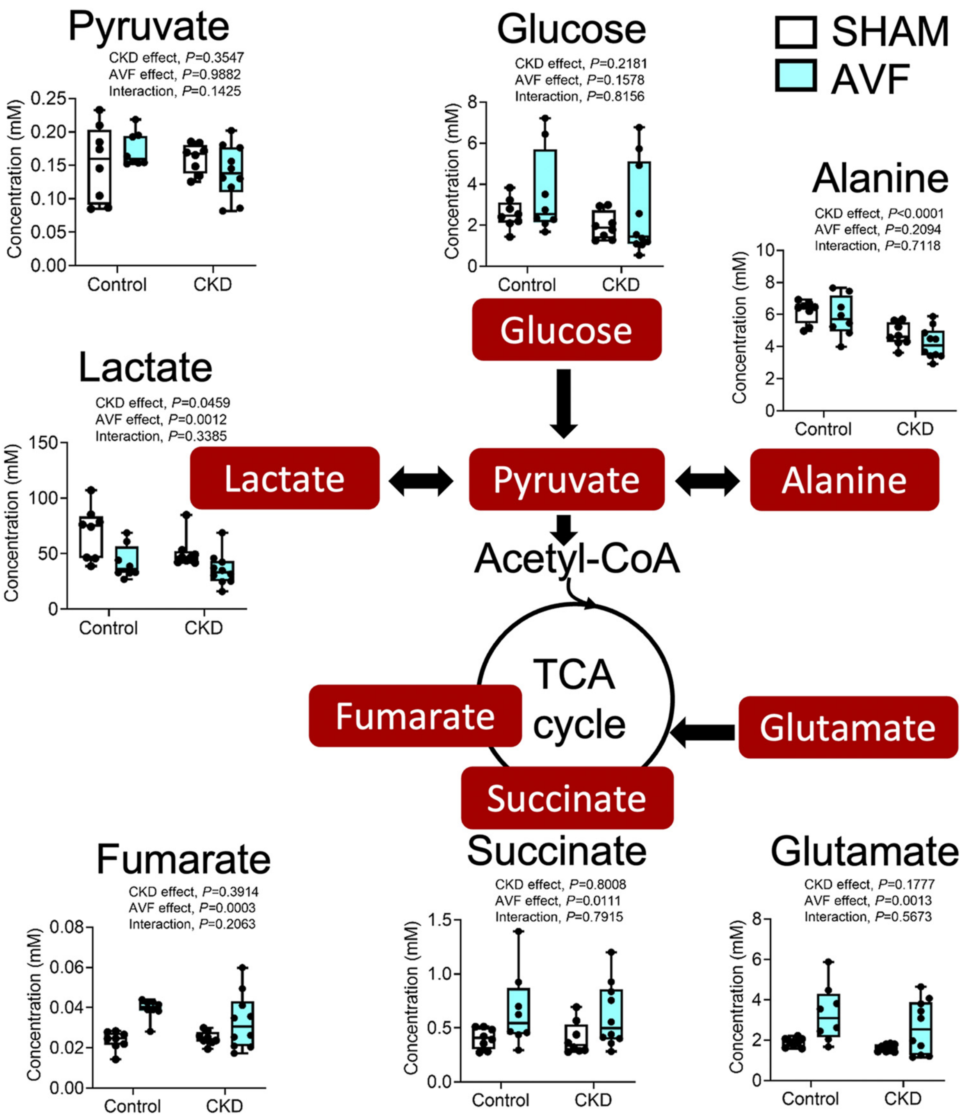

Figure 5. Graphical depiction for glycolytic and tricarboxylic acid (TCA) cycle metabolites in skeletal muscle (quadriceps) with quantified metabolites shown as box and whisker plots (with 95% confidence intervals) in chronic kidney disease (CKD) arteriovenous fistula (AVF) (n = 10), CKD sham (n = 10), control (CON) AVF (n = 8), and CON sham (n = 7) groups. The y-axis is the concentration (in mM). Statistical analysis was performed using two-way ANOVA.

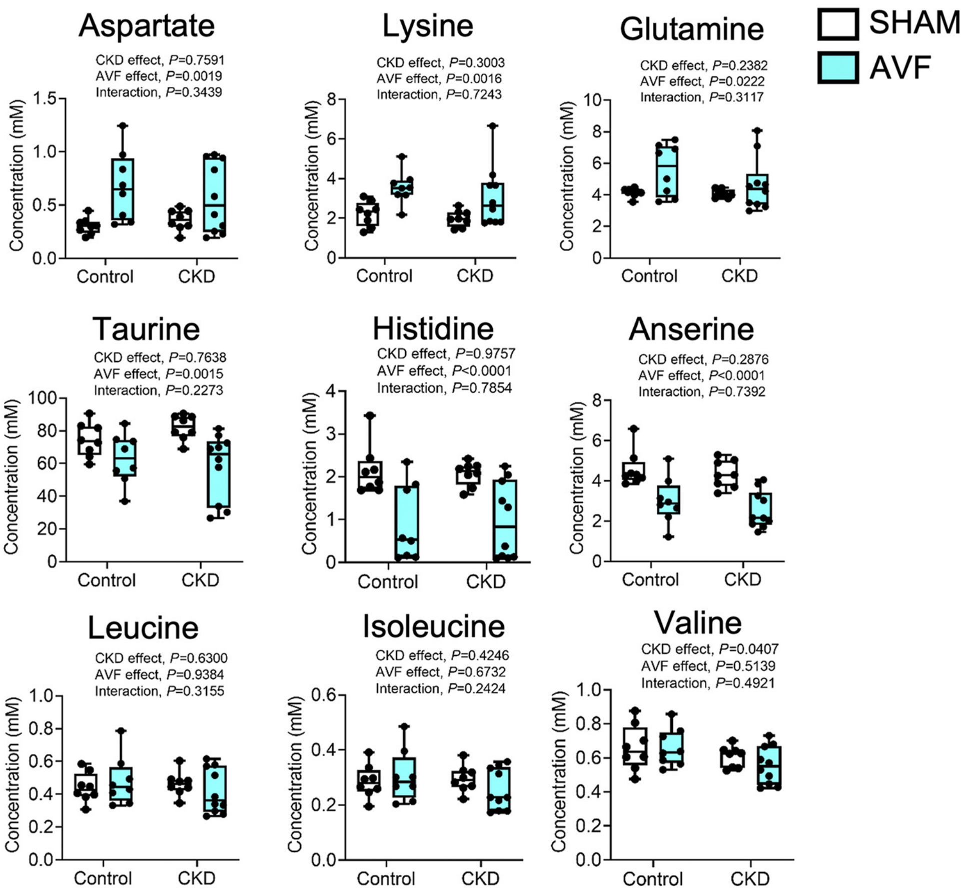

Figure 6. Alterations in amino acid profiles following arteriovenous fistula (AVF) placement. Data are presented as box and whisker plots (with 95% confidence intervals) in chronic kidney disease (CKD) arteriovenous fistula (AVF) (n = 10), CKD sham (n = 10), control (CON) AVF (n = 8), and CON sham (n = 7) groups. Statistical testing was performed with two-way ANOVA.

Pearson correlation coefficients between metabolite abundances and limb functional outcomes including grip strength, gait speed, and mitochondrial respiratory capacity. As shown in Table 2, several metabolites detected in the aqueous phase displayed strong (high Pearson r value) and significant associations with limb functional outcomes. Table 3 shows that ∼50% of metabolites detected in the organic phase displayed strong (high Pearson r value) and significant associations with limb functional outcomes. To evaluate the level of variance in functional outcomes explained by metabolite changes, stepwise multiple linear regression models were examined (summarized in Table 4). The results of these analyses suggested that 92% of variance in grip strength may be accounted for by differences in the abundance of five aqueous and lipid phase metabolites: (CH_2-CH=CH-CH_2) α-methylene protons, (CH_2-CH_2-COO-) β-methylene protons, alanine, anserine, and glutamine. Regarding gait speed, 88% of the variance was accounted for by three aqueous phase metabolites (creatine, pantothenate, and ATP). Fewer metabolites were found to explain variance in mitochondrial respiration. Aqueous phase metabolites (anserine and phenylalanine) were found to account for 62% of variance in the maximal respiration rate in isolated skeletal muscle mitochondria.

DISCUSSION

Obtaining durable and functional hemodialysis access remains a top priority for the treatment of ESKD. Creation of an AVF remains the preferred conduit to achieve this goal as the long-term performance is more favorable than arteriovenous grafts or tunneled dialysis catheter placement. A

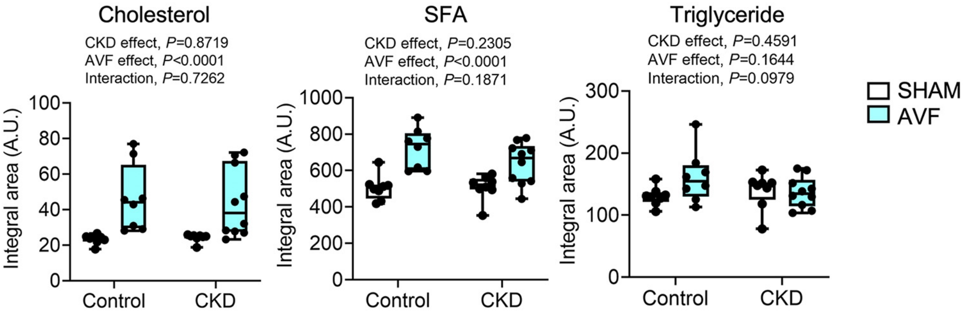

Figure 7. Accumulation of cholesterol and saturated fatty acids in muscle after arteriovenous fistula (AVF) creation. Data are presented as box and whisker plots (with 95% confidence intervals) in chronic kidney disease (CKD) arteriovenous fistula (AVF) (n = 10), CKD sham (n = 10), control (CON) AVF (n = 8), and CON sham (n = 7) groups. Statistical analysis was performed using two-way ANOVA. AU, arbitrary units; SFA, saturated fatty acids.

Table 2. *Pearson correlation analysis of aqueous phase metabolites and limb functional outcomes*

	Grip Strength		Gait Speed		Respiratory Capacity	
Metabolite	**Pearson *r***	***P* Value**	**Pearson *r***	***P* Value**	**Pearson *r***	***P* Value**
Anserine	0.6995*	<0.0001*	0.6191*	0.0007*	0.7439*	<0.0001*
Aspartate	−0.7719*	<0.0001*	−0.781*	<0.0001*	−0.5902*	0.0015*
Trimethylamine	0.772*	<0.0001*	0.7997*	<0.0001*	0.4956*	0.01*
Taurine	0.7346*	<0.0001*	0.8483*	<0.0001*	0.4458*	0.0225*
Histidine	0.8388*	<0.0001*	0.8636*	<0.0001*	0.5647*	0.0027*
Glutamate1	−0.7464*	<0.0001*	−0.7596*	<0.0001*	−0.5556*	0.0032*
Creatine	0.7868*	<0.0001*	0.8743*	<0.0001*	0.5181*	0.0067*
ATP	0.6492*	0.0003*	0.6809*	0.0001*	0.4901*	0.011*
Pantothenate	−0.6385*	0.0004*	−0.6247*	0.0006*	−0.4453*	0.0226*
AMP	0.6362*	0.0005*	0.6714*	0.0002*	0.4829*	0.0125*
Lactate	0.6222*	0.0007*	0.5533*	0.0034*	0.4122*	0.0364*
IMP	−0.5663*	0.0026*	−0.5012*	0.0091*	−0.4209*	0.0323*
Glucose	−0.554*	0.0033*	−0.6526*	0.0003*	−0.3968*	0.0448*
Phenylalanine	−0.5274*	0.0056*	−0.5543*	0.0033*	−0.4495*	0.0212*
NAD +	0.5189*	0.0066*	0.6109*	0.0009*	0.3615	0.0696
Alanine	0.5145*	0.0072*	0.5105*	0.0077*	0.1476	0.4718
Glutamine	−0.5042*	0.0086*	−0.372	0.0613	−0.3525	0.0774
Nicotinurate	0.492*	0.0107*	0.3822	0.054	0.4943*	0.0103
Creatinine + PCr	0.4392*	0.0248*	0.5356*	0.0048*	0.2681	0.1854
Leucine	−0.4184*	0.0334*	−0.5453*	0.004*	−0.2544	0.2099
Isoleucine	−0.3925*	0.0473*	−0.4997*	0.0093*	−0.2217	0.2765
Mannose	0.3666	0.0655	0.453	0.0201*	0.1942	0.3417
Fumarate	−0.3624	0.0688	−0.1942	0.3418	−0.3274	0.1025
2-Hydroxyvalerate	−0.3473	0.0821	−0.4856*	0.0119*	−0.1657	0.4186
Isobutyrate	−0.3465	0.0829	−0.2733	0.1768	−0.1935	0.3435
Allantoin	−0.3383	0.091	−0.3005	0.1357	−0.3229	0.1076
Tyrosine	−0.2828	0.1615	−0.2634	0.1935	−0.1157	0.5734
Valine	−0.2079	0.3082	−0.3194	0.1117	−0.1258	0.5404
Lysine	−0.186	0.363	−0.07086	0.7309	−0.3849	0.0522
Acetate	−0.143	0.486	−0.1142	0.5787	−0.2256	0.2678
Pyruvate	−0.1168	0.5698	−0.07877	0.7021	−0.03559	0.863
Glycerol	−0.1016	0.6213	−0.1269	0.5367	−0.1278	0.5338
Succinate	0.07867	0.7025	0.09255	0.6529	−0.2988	0.1382
Glycine	0.0774	0.7071	0.003244	0.9875	−0.134	0.514
Formate	−0.07547	0.714	−0.1784	0.3831	0.2135	0.2949
Tryptophan	0.02647	0.8979	−0.0245	0.9054	0.1813	0.3755
Benzoate	0.01528	0.9409	−0.004184	0.9838	0.1013	0.6226

*Statistical significance.

significant proportion of patients that receive an AVF report unfavorable side effects contributing to reduced hand function. Unfortunately, treatment options are limited to various forms of surgical remediation or access ligation, which is reserved for severe cases. Therefore, a majority of patients with ARHD have persistent but varying degrees of hand disability, ranging from mild sensory or motor deficits to pain and weakness. Notably, hemodynamic changes alone do not explain the majority of ARHD cases (3) due to poor correlation with the heterogeneous clinical phenotype. Importantly, very little is known about the additional underlying mechanisms that contribute to this complex and potentially devastating clinical problem. Accordingly, the objective of the present study was to examine alterations in the muscle metabolome that contribute to functional limb outcomes following AVF creation in a murine iliac AVF model (18).

A defining feature uncovered in our analyses was that AVF creation, independent of the presence or absence of CKD, resulted in a clear energetic stress within the skeletal muscle distal to the AVF. AVF creation resulted in lower levels of key energetic metabolites ATP, AMP, and creatine, which coincided with increased levels of IMP. The mitochondrion is a key organelle responsible for driving the synthesis of ATP through a process known as oxidative phosphorylation. Unfortunately, CKD alone impairs mitochondrial oxidative phosphorylation (7, 36–39), and herein we report that AVF creation further impairs oxidative phosphorylation. Of further concern, our results show that AVF creation decreased lactate levels without changing glucose or pyruvate concentrations, suggesting that both oxidative metabolism and glycolysis are impaired following AVF creation. It is important to consider that these metabolic changes occurred in the presence of mild ischemia, measured with laser-Doppler flowmetry, but did not cause overt muscle atrophy. Taken together, these findings indicate that disturbed muscle energetics is a critical pathological feature of the limb muscle distal to AVF creation, and thus interventions to protect or improve muscle metabolism with AVF placement warrant further exploration.

Interestingly, muscle from AVF mice also demonstrated a substantial increase in cholesterol and saturated fatty acid levels (Fig. 7 and Supplemental Table S1). Correlation and multiple regression analyses identified cholesterol changes as negative influences on grip strength, gait speed, and mitochondrial respiratory function. In contrast to cholesterol and saturated fatty acids, levels of phospholipids and triglycerides were similar across all groups. The accumulation of

Table 3. *Pearson correlation analysis of organic phase metabolites and limb functional outcomes*

	Grip Strength		Gait Speed		Respiratory Capacity	
Metabolite	Pearson *r*	*P* Value	Pearson *r*	*P* Value	Pearson *r*	*P* Value
(CH$_3$) cholesterol/cholesterol ester (C18)	−0.826*	<0.0001*	−0.8355*	<0.0001*	−0.8556*	<0.0001*
(n-3)CH$_3$ fatty acids	−0.8137*	<0.0001*	−0.7222*	<0.0001*	−0.7721*	<0.0001*
(CH$_3$) cholesterol (C19)	−0.8192*	<0.0001*	−0.8264*	<0.0001*	−0.8489*	<0.0001*
(CH$_2$)$_n$ of aliphatic chains	−0.7674*	<0.0001*	−0.6521*	0.0003*	−0.7038*	<0.0001*
(C**H**$_2$-CH=CH-CH$_2$) α-methylene protons	−0.7905*	<0.0001*	−0.6533*	0.0003*	−0.71*	<0.0001*
(C**H$_2$**-CCO-) α-methylene protons	−0.6854*	0.0001*	−0.5283*	0.0055*	−0.584*	0.0017*
Unknown triplet	0.6664*	0.0002*	0.7156*	<0.0001*	0.6694*	0.0002*
(C**H**$_2$-CH$_2$-COO-) β-methylene protons	−0.6469*	0.0004*	−0.5023*	0.0089*	−0.5879*	0.0016*
(CH$_2$)$_n$ of Cholesterol	−0.6382*	0.0005*	−0.4513*	0.0207*	−0.5489*	0.0037*
(=CH-C**H$_2$**-CH=CH)divinyl methylene protons	0.5569*	0.0031*	0.7257*	<0.0001*	0.6262*	0.0006*
CH TG	−0.2146	0.2925	−0.3007	0.1355	−0.233	0.2521
3CH$_2$ glycerophospholipids	0.1858	0.3635	0.4284*	0.029*	0.248	0.222
Cholesterol 3	−0.1665	0.4163	−0.2834	0.1606	−0.2321	0.2539
CH=CH	0.1598	0.4354	0.4069*	0.0391*	0.2766	0.1714
CH$_2$ of TG2	−0.1558	0.4473	0.03159	0.8782	−0.03964	0.8476
N$^+$(C**H$_3$**)$_3$	0.1199	0.5595	0.3576	0.0729	0.2225	0.2746
Cholesterol2	−0.1048	0.6105	−0.02424	0.9064	−0.2034	0.319
CH$_2$ of TG1	−0.08009	0.6973	0.04576	0.8243	−0.01909	0.9263
CH phospholipid	0.0242	0.9066	0.2877	0.1541	0.1648	0.4211
1CH phospholipids + TG	0.008512	0.9671	0.2532	0.212	0.1406	0.4933

TG, triglyceride.*Statistical significance.

lipids within muscle, termed myosteatosis, negatively correlates with muscle mass, strength, and metabolic health (40). Although the mechanisms driving ectopic fat deposition following AVF creation are unclear, previous work in other diseases has suggested that fibroadipogenic progenitor cells may be the primary resident stem cell responsible (41). Furthermore, myosteatosis has also been linked to inflammation and sarcopenia (42), both common characteristics of patients with CKD. Regrettably, a limitation of ^{1}H NMR, which measures proton spin resonance, is that it is not able to identify specific species of these fatty acids. Considering that both the composition and subcellular localization of lipids are believed to influence muscle health (43, 44), future studies are needed to uncover the role of myosteatosis in ARHD.

The present study has some limitations that warrant discussion. First, adenine-supplemented chow was used to induce renal impairment in mice. Although this is an established model of CKD, the duration of adenine feeding was relatively short (28 days) and the severity of renal dysfunction may not fully represent ESKD. Accordingly, there were fewer effects of CKD alone on the skeletal muscle metabolome compared with those observed with longer duration adenine feeding (6 mo) (5). Second, only young male mice were used in the present study, although the prevalence of ESKD is associated with older age and is common in women as well. Future studies are needed to address the impact of biological sex and age on the murine iliac AVF model. Third, we performed metabolomics using NMR-based technologies, which is highly regarded for its accuracy but has lower sensitivity compared with mass spectrometry. Therefore, less concentrated metabolites were not detectable in this study but could be related to the limb pathophysiology following AVF creation and ARHD. Fourth, metabolite extractions were performed from the quadriceps muscle, but hemodynamic measures of limb perfusion were performed on the more distal TA muscle. In our experience, the anatomic location and presence of a subcutaneous fat pad overlying the quadricep muscles are barriers to producing reliable perfusion with laser-Doppler flowmetry. Similarly,

Table 4. *Results of multiple linear regression models for limb function outcomes*

	B	Standard Error	β	*P* Value	Partial R^2	Tolerance	VIF	Model R^2	Adjusted R^2
Model: grip strength									
(Constant)	88.21	18.62		0.000				0.943	0.928
(C**H**$_2$-CH=CH-CH$_2$) α-methylene protons	−1.02	0.18	−1.729	0.000	−0.307	0.03	31.75		
Alanine	9.93	1.74	0.330	0.000	0.306	0.86	1.17		
Anserine	6.50	2.72	0.177	0.027	0.524	0.52	1.91		
(C**H**$_2$-CH$_2$-COO-) β-methylene protons	0.83	0.22	0.984	0.001	0.043	0.04	22.99		
Glutamine	4.64	2.45	0.161	0.073	0.393	0.39	2.55		
Model: gait speed									
(Constant)	8.67	1.34		0.000				0.899	0.885
Creatine	0.44	0.06	1.047	0.000	0.842	0.23	4.44		
Pantothenate	−23.49	4.93	−0.347	0.000	−0.712	0.87	1.16		
ATP	−1.69	0.69	−0.344	0.023	−0.463	0.24	4.26		
Model: mitochondrial respiratory capacity									
(Constant)	3,466.5	3,243.9		0.296				0.658	0.628
Anserine	2,843.0	513.8	0.686	0.000	0.746	0.97	1.03		
Phenylalanine	−40,515.4	15,299.6	−0.328	0.014	−0.483	0.97	10.3		

other functional outcomes within our analyses involved other hindlimb muscles, a feature that stems from the limited tissue available from the unilateral surgical limb of a mouse. Finally, a limitation of all metabolomics studies stems from the fact that our detected concentrations of metabolites represent a snapshot of biochemical systems that are in a constant state of flux. As such, experimental factors such as processing time, buffer composition, and temperatures during extraction can impact tissue enzyme activity. Furthermore, the isoflurane anesthetic used in this study has been shown to impair mitochondrial oxidative phosphorylation through inhibition of complex I (45–48). These experimental factors likely contribute to the lower than expected ATP concentrations (∼3.2 mM) observed in muscle from sham animals in this study.

Conclusions

In this study, NMR-based metabolomic profiling was performed on limb muscle obtained distal to iliac AVF creation in mice with and without CKD. Regardless of the presence or absence of renal dysfunction, AVF creation resulted in profound energetic stress as indicated by reduced levels of ATP, AMP, and creatine as well as increased levels of IMP, all indicative of an imbalance between energy utilization and synthesis. Moreover, AVF creation significantly increased the levels of saturated fatty acids and cholesterols in muscle, suggesting the possible development of myosteatosis. Consistent with the neuromotor impairments in patients with ARHD (i.e., weakness), these metabolic changes have been linked to muscle impairment in other conditions such as aging and diabetes. These observations suggest that interventions, such as exercise, should be considered as a means of reducing ARHD in patients with ESKD.

DATA AVAILABILITY

All NMR data associated with this study are available in Metabolomics Workbench under the following Study ID numbers: ST002188 and ST002189.

SUPPLEMENTAL DATA

Supplemental Figs. S1−S7 and Supplemental Table S1: https://doi.org/10.6084/m9.figshare.20000153.v2.

ACKNOWLEDGMENTS

The NMR portion of this study was conducted in the McKnight Brain Institute at the National High Magnetic Field Laboratory's Advanced Magnetic Resonance Imaging and Spectroscopy Facility, which is further supported by National Science Foundation Cooperative Agreement No. DMR-1644779 and the State of Florida.

GRANTS

This work was supported by National Institutes of Health (NIH) Grant R01HL148597 (to S.T.S.). Additional salary support was provided by NIH Grants R01DK119274 (to S.A.B.) and R01HL149704 (to T.E.R.) and by American Heart Association Postdoctoral Fellowship POST903198 (to K. K).

DISCLOSURES

No conflicts of interest, financial or otherwise, are declared by the authors.

AUTHOR CONTRIBUTIONS

R.B.K., K.K., T.A.C., K.A.O., S.A.B., S.T.S., and T.E.R. conceived and designed research; R.B.K., K.K., E.M.A., B.F., K.C.H., Q.H., V.R.P., and T.A.C. performed experiments; R.B.K., K.K., E.M.A., K.C.H., Q.H., V.R.P., T.A.C., and T.E.R. analyzed data; R.B.K., K.K., E.M.A., B.F., K.C.H., Q.H., V.R.P., T.A.C., K.A.O., S.A.B., S.T.S., and T.E.R. interpreted results of experiments; R.B.K., K.K., and T.E.R. prepared figures; R.B.K., K.K., E.M.A., S.A.B., S.T.S., and T.E.R. drafted manuscript; R.B.K., K.K., E.M.A., B.F., K.C.H., Q.H., V.R.P., T.A.C., K.A.O., S.A.B., S.T.S., and T.E.R. edited and revised manuscript; R.B.K., K.K., E.M.A., B.F., K.C.H., Q.H., V.R.P., T.A.C., K.A.O., S.A.B., S.T.S., and T.E.R. approved final version of manuscript.

REFERENCES

1. **Johansen KL**, **Chertow GM**, **Foley RN**, **Gilbertson DT**, **Herzog CA**, **Ishani A**, **Israni AK**, **Ku E**, **Kurella Tamura M**, **Li S**, **Li S**, **Liu J**, **Obrador GT**, **O'Hare AM**, **Peng Y**, **Powe NR**, **Roetker NS**, **St Peter WL**, **Abbott KC**, **Chan KE**, **Schulman IH**, **Snyder J**, **Solid C**, **Weinhandl ED**, **Winkelmayer WC**, **Wetmore JB.** US Renal Data System 2020 Annual Data Report: epidemiology of kidney disease in the United States. *Am J Kidney Dis* 77: A7–A8, 2021. doi:10.1053/j.ajkd.2021.01.002.
2. **Bao Y-W**, **Yuan Y**, **Chen J-H**, **Lin W-Q.** Kidney disease models: tools to identify mechanisms and potential therapeutic targets. *Zool Res* 39: 72–86, 2018. doi:10.24272/j.issn.2095-8137.2017.055.
3. **Rehfuss JP**, **Berceli SA**, **Barbey SM**, **He Y**, **Kubilis PS**, **Beck AW**, **Huber TS**, **Scali ST.** The spectrum of hand dysfunction after hemodialysis fistula placement. *Kidney Int Rep* 2: 332–341, 2017. doi:10.1016/j.ekir.2016.11.006.
4. **Schmidt CA**, **Ryan TE**, **Lin CT**, **Inigo MMR**, **Green TD**, **Brault JJ**, **Spangenburg EE**, **McClung JM.** Diminished force production and mitochondrial respiratory deficits are strain-dependent myopathies of subacute limb ischemia. *J Vasc Surg* 65: 1504–1514.e11, 2017. doi:10.1016/j.jvs.2016.04.041.
5. **Khattri RB**, **Thome T**, **Ryan TE.** Tissue-specific H-1-NMR metabolomic profiling in mice with adenine-induced chronic kidney disease. *Metabolites* 11: 45, 2021. doi:10.3390/metabo11010045.
6. **Kim K**, **Anderson EM**, **Thome T**, **Lu G**, **Salyers ZR**, **Cort TA**, **O'Malley KA**, **Scali ST**, **Ryan TE.** Skeletal myopathy in CKD: a comparison of adenine-induced nephropathy and 5/6 nephrectomy models in mice. *Am J Physiol Renal Physiol* 321: F106–F119, 2021. doi:10.1152/ajprenal.00117.2021.
7. **Thome T**, **Kumar RA**, **Burke SK**, **Khattri RB**, **Salyers ZR**, **Kelley RC**, **Coleman MD**, **Christou DD**, **Hepple RT**, **Scali ST**, **Ferreira LF**, **Ryan TE.** Impaired muscle mitochondrial energetics is associated with uremic metabolite accumulation in chronic kidney disease. *JCI Insight* 6: e139826, 2021. doi:10.1172/jci.insight.139826.
8. **Berru FN**, **Gray SE**, **Thome T**, **Kumar RA**, **Salyers ZR**, **Coleman M**, **Dennis L**, **O'Malley K**, **Ferreira LF**, **Berceli SA**, **Scali ST**, **Ryan TE.** Chronic kidney disease exacerbates ischemic limb myopathy in mice via altered mitochondrial energetics. *Sci Rep* 9: 15547, 2019. doi:10.1038/s41598-019-52107-7.
9. **Sczelecki S**, **Besse-Patin A**, **Abboud A**, **Kleiner S**, **Laznik-Bogoslavski D**, **Wrann CD**, **Ruas JL**, **Haibe-Kains B**, **Estall JL.** Loss of Pgc-1 alpha expression in aging mouse muscle potentiates glucose intolerance and systemic inflammation. *Am J Physiol Endocrinol Metab* 306: E157–E167, 2014. doi:10.1152/ajpendo.00578.2013.
10. **Garcia S**, **Nissanka N**, **Mareco EA**, **Rossi S**, **Peralta S**, **Diaz F**, **Rotundo RL**, **Carvalho RF**, **Moraes CT.** Overexpression of PGC-1 alpha in aging muscle enhances a subset of young-like molecular patterns. *Aging cell* 17: e12707, 2018. doi:10.1111/acel.12707.
11. **Ubaida-Mohien C**, **Lyashkov A**, **Gonzalez-Freire M**, **Tharakan R**, **Shardell M**, **Moaddel R**, **Semba RD**, **Chia CW**, **Gorospe M**, **Sen R**, **Ferrucci L.** Discovery proteomics in aging human skeletal muscle

finds change in spliceosome, immunity, proteostasis and mitochondria. *Elife* 8: e49874, 2019. doi:10.7554/eLife.49874.

12. **Anagnostou ME**, **Hepple RT.** Mitochondrial mechanisms of neuromuscular junction degeneration with aging. *Cells* 9: 197, 2020. doi:10.3390/cells9010197.
13. **Yang BX**, **Shergill U**, **Fu AA**, **Knudsen B**, **Misra S.** The mouse arteriovenous fistula model. *J Vasc Interv Radiol* 20: 946–950, 2009. doi:10.1016/j.jvir.2009.03.044.
14. **Misra S**, **Shergill U**, **Yang BX**, **Janardhanan R**, **Misra KD.** Increased expression of HIF-1 α, VEGF-A and its receptors, MMP-2, TIMP-1, and ADAMTS-1 at the venous stenosis of arteriovenous fistula in a mouse model with renal insufficiency. *J Vasc Interv Radiol* 21: 1255–1261, 2010. doi:10.1016/j.jvir.2010.02.043.
15. **Yamamoto K**, **Protack CD**, **Tsuneki M**, **Hall MR**, **Wong DJ**, **Lu DY**, **Assi R**, **Williams WT**, **Sadaghianloo N**, **Bai HL**, **Miyata T**, **Madri JA**, **Dardik A.** The mouse aortocaval fistula recapitulates human arteriovenous fistula maturation. *Am J Physiol Heart Circ Physiol* 305: H1718–H1725, 2013. doi:10.1152/ajpheart.00590.2013.
16. **Kang L**, **Grande JP**, **Hillestad ML**, **Croatt AJ**, **Barry MA**, **Katusic ZS**, **Nath KA.** A new model of an arteriovenous fistula in chronic kidney disease in the mouse: beneficial effects of upregulated heme oxygenase-1. *Am J Physiol Renal Physiol* 310: F466–F476, 2016. doi:10.1152/ajprenal.00288.2015.
17. **Wong CY**, **de Vries MR**, **Wang Y**, **van der Vorst JR**, **Vahrmeijer AL**, **van Zonneveld AJ**, **Hamming JF**, **Roy-Chaudhury P**, **Rabelink TJ**, **Quax PHA**, **Rotmans JI.** A novel murine model of arteriovenous fistula failure: the surgical procedure in detail. *J Vis Exp*, 2016. doi:10.3791/53294.
18. **Kim K**, **Anderson EM**, **Martin AJ**, **Hu Q**, **Cort TA**, **Harland KC**, **O'Malley KA**, **Lu G**, **Berceli SA**, **Ryan TE**, **Scali ST.** Development of a murine iliac arteriovenous fistula model for examination of hemodialysis access-related limb pathophysiology. *JVS Vasc Sci* 2: 247–259, 2021. doi:10.1016/j.jvssci.2021.09.022.
19. **Thome T**, **Salyers ZR**, **Kumar RA**, **Hahn D**, **Berru FN**, **Ferreira LF**, **Scali ST**, **Ryan TE.** Uremic metabolites impair skeletal muscle mitochondrial energetics through disruption of the electron transport system and matrix dehydrogenase activity. *Am J Physiol Cell Physiol* 317: C701–C713, 2019. doi:10.1152/ajpcell.00098.2019.
20. **Thome T**, **Coleman MD**, **Ryan TE.** Mitochondrial bioenergetic and proteomic phenotyping reveals organ-specific consequences of chronic kidney disease in mice. *Cells* 10: 3282, 2021. doi:10.3390/cells10123282.
21. **Qi Z**, **Whitt I**, **Mehta A**, **Jin J**, **Zhao M**, **Harris RC**, **Fogo AB**, **Breyer MD.** Serial determination of glomerular filtration rate in conscious mice using FITC-inulin clearance. *Am J Physiol Renal Physiol* 286: F590–F596, 2004. doi:10.1152/ajprenal.00324.2003.
22. **Mayeuf-Louchart A**, **Hardy D**, **Thorel Q**, **Roux P**, **Gueniot L**, **Briand D**, **Mazeraud A**, **Bougle A**, **Shorte SL**, **Staels B**, **Chretien F**, **Duez H**, **Danckaert A.** MuscleJ: a high-content analysis method to study skeletal muscle with a new Fiji tool. *Skelet Muscle* 8: 25, 2018. doi:10.1186/s13395-018-0171-0.
23. **Folch J**, **Lees M**, **Sloane Stanley GH.** A simple method for the isolation and purification of total lipides from animal tissues. *J Biol Chem* 226: 497–509, 1957.
24. **Khattri RB**, **Kim K**, **Thome T**, **Salyers ZR**, **O'Malley KA**, **Berceli SA**, **Scali ST**, **Ryan TE.** Unique metabolomic profile of skeletal muscle in chronic limb threatening ischemia. *J Clin Med* 10: 548, 2021. doi:10.3390/jcm10030548.
25. **Ravanbakhsh S**, **Liu P**, **Bjorndahl TC**, **Mandal R**, **Grant JR**, **Wilson M**, **Eisner R**, **Sinelnikov I**, **Hu X**, **Luchinat C**, **Greiner R**, **Wishart DS.** Correction: accurate, fully-automated NMR spectral profiling for metabolomics. *PLoS One* 10: e0132873, 2015. doi:10.1371/journal.pone.0132873.
26. **Myer C**, **Abdelrahman L**, **Banerjee S**, **Khattri RB**, **Merritt ME**, **Junk AK**, **Lee RK**, **Bhattacharya SK.** Aqueous humor metabolite profile of pseudoexfoliation glaucoma is distinctive. *Mol Omics* 16: 425–435, 2020. doi:10.1039/c9mo00192a.
27. **Krssak M**, **Lindeboom L**, **Schrauwen-Hinderling V**, **Szczepaniak L**, **Derave W**, **Lundbom J**, **Befroy D**, **Schick F**, **Machann J**, **Kreis R**, **Boesch C.** Proton magnetic resonance spectroscopy in skeletal muscle: experts' consensus recommendations. *NMR Biomed* 34: e4266, 2021. doi:10.1002/nbm.4266.
28. **Srivastava NK**, **Pradhan S**, **Mittal B**, **Gowda GA.** High resolution NMR based analysis of serum lipids in Duchenne muscular dystrophy patients and its possible diagnostic significance. *NMR Biomed* 23: 13–22, 2010. doi:10.1002/nbm.1419.
29. **Ulrich EL**, **Akutsu H**, **Doreleijers JF**, **Harano Y**, **Ioannidis YE**, **Lin J**, **Livny M**, **Mading S**, **Maziuk D**, **Miller Z**, **Nakatani E**, **Schulte CF**, **Tolmie DE**, **Kent Wenger R**, **Yao H**, **Markley JL.** BioMagResBank. *Nucleic Acids Res* 36: D402–D408, 2008. doi:10.1093/nar/gkm957.
30. **Zhao Y**, **Liu J**, **Cheng X**, **Bai X**, **Lin R.** Urinary metabonomics study on biochemical changes in an experimental model of chronic renal failure by adenine based on UPLC Q-TOF/MS. *Clin Chim Acta* 413: 642–649, 2012. doi:10.1016/j.cca.2011.12.014.
31. **Nguy L**, **Johansson ME**, **Grimberg E**, **Lundgren J**, **Teerlink T**, **Carlström M**, **Lundberg JO**, **Nilsson H**, **Guron G.** Rats with adenine-induced chronic renal failure develop low-renin, salt-sensitive hypertension and increased aortic stiffness. *Am J Physiol Regul Integr Comp Physiol* 304: R744–R752, 2013. doi:10.1152/ajpregu.00562.2012.
32. **Babizhayev MA**, **Seguin MC**, **Gueyne J**, **Evstigneeva RP**, **Ageyeva EA**, **Zheltukhina GA.** L-Carnosine (β-alanyl-L-histidine) and carcinine (β-alanylhistamine) act as natural antioxidants with hydroxyl-radical-scavenging and lipid-peroxidase activities. *Biochem J* 304: 509–516, 1994. doi:10.1042/bj3040509.
33. **Chan WK**, **Decker EA**, **Chow CK**, **Boissonneault GA.** Effect of dietary carnosine on plasma and tissue antioxidant concentrations and on lipid oxidation in rat skeletal muscle. *Lipids* 29: 461–466, 1994. doi:10.1007/BF02578242.
34. **Zhang J**, **Wang YT**, **Miller JH**, **Day MM**, **Munger JC**, **Brookes PS.** Accumulation of succinate in cardiac ischemia primarily occurs via canonical Krebs cycle activity. *Cell Rep* 23: 2617–2628, 2018. doi:10.1016/j.celrep.2018.04.104.
35. **Chouchani ET**, **Pell VR**, **Gaude E**, **Aksentijevic D**, **Sundier SY**, **Robb EL**, **Logan A**, **Nadtochiy SM**, **Ord EN**, **Smith AC**, **Eyassu F**, **Shirley R**, **Hu CH**, **Dare AJ**, **James AM**, **Rogatti S**, **Hartley RC**, **Eaton S**, **Costa AS**, **Brookes PS**, **Davidson SM**, **Duchen MR**, **Saeb-Parsy K**, **Shattock MJ**, **Robinson AJ**, **Work LM**, **Frezza C**, **Krieg T**, **Murphy MP.** Ischaemic accumulation of succinate controls reperfusion injury through mitochondrial ROS. *Nature* 515: 431–435, 2014. doi:10.1038/nature13909.
36. **Gamboa JL**, **Roshanravan B**, **Towse T**, **Keller CA**, **Falck AM**, **Yu C**, **Frontera WR**, **Brown NJ**, **Ikizler TA.** Skeletal muscle mitochondrial dysfunction is present in patients with CKD before initiation of maintenance hemodialysis. *Clin J Am Soc Nephrol* 15: 926–936, 2020. doi:10.2215/CJN.10320819.
37. **Kestenbaum B**, **Gamboa J**, **Liu S**, **Ali AS**, **Shankland E**, **Jue T**, **Giulivi C**, **Smith LR**, **Himmelfarb J**, **de Boer IH**, **Conley K**, **Roshanravan B.** Impaired skeletal muscle mitochondrial bioenergetics and physical performance in chronic kidney disease. *JCI Insight* 5: e133289, 2020. doi:10.1172/jci.insight.133289.
38. **Watson EL**, **Baker LA**, **Wilkinson TJ**, **Gould DW**, **Graham-Brown MPM**, **Major RW**, **Ashford RU**, **Philp A**, **Smith AC.** Reductions in skeletal muscle mitochondrial mass are not restored following exercise training in patients with chronic kidney disease. *FASEB J* 34: 1755–1767, 2020. doi:10.1096/fj.201901936RR.
39. **Xu CQ**, **Kasimumali A**, **Guo XJ**, **Lu RH**, **Xie KW**, **Zhu ML**, **Qian YY**, **Chen XH**, **Pang HH**, **Wang Q**, **Fan ZP**, **Dai HL**, **Mou S**, **Ni ZH**, **Gu LY.** Reduction of mitochondria and up regulation of pyruvate dehydrogenase kinase 4 of skeletal muscle in patients with chronic kidney disease. *Nephrology (Carlton)* 25: 230–238, 2020. doi:10.1111/nep.13606.
40. **Nachit M**, **De Rudder M**, **Thissen JP**, **Schakman O**, **Bouzin C**, **Horsmans Y**, **Vande Velde G**, **Leclercq IA.** Myosteatosis rather than sarcopenia associates with non-alcoholic steatohepatitis in non-alcoholic fatty liver disease preclinical models. *J Cachexia Sarcopenia Muscle* 12: 144–158, 2021. doi:10.1002/jcsm.12646.
41. **Uezumi A**, **Ito T**, **Morikawa D**, **Shimizu N**, **Yoneda T**, **Segawa M**, **Yamaguchi M**, **Ogawa R**, **Matev MM**, **Miyagoe-Suzuki Y**, **Takeda S**, **Tsujikawa K**, **Tsuchida K**, **Yamamoto H**, **Fukada S.** Fibrosis and adipogenesis originate from a common mesenchymal progenitor in skeletal muscle. *J Cell Sci* 124: 3654–3664, 2011. doi:10.1242/jcs.086629.
42. **Li CW**, **Yu K**, **Shyh-Chang N**, **Jiang ZM**, **Liu TY**, **Ma SL**, **Luo LF**, **Guang L**, **Liang K**, **Ma WW**, **Miao HF**, **Cao WH**, **Liu RR**, **Jiang LJ**, **Yu SL**, **Li C**, **Liu HJ**, **Xu LY**, **Liu RJ**, **Zhang XY**, **Liu GS.** Pathogenesis of sarcopenia and the relationship with fat mass: descriptive review. *J Cachexia Sarcopenia Muscle* 13: 781–794, 2022. doi:10.1002/jcsm.12901.

43. **Bergman BC**, **Goodpaster BH.** Exercise and muscle lipid content, composition, and localization: influence on muscle insulin sensitivity. *Diabetes* 69: 848–858, 2020. doi:10.2337/dbi18-0042.
44. **Sparks LM**, **Goodpaster BH**, **Bergman BC.** The metabolic significance of intermuscular adipose tissue: is IMAT a friend or a foe to metabolic health? *Diabetes* 70: 2457–2467, 2021. doi:10.2337/dbi19-0006.
45. **Ljubkovic M**, **Mio Y**, **Marinovic J**, **Stadnicka A**, **Warltier DC**, **Bosnjak ZJ**, **Bienengraeber M.** Isoflurane preconditioning uncouples mitochondria and protects against hypoxia-reoxygenation. *Am J Physiol Cell Physiol* 292: C1583–C1590, 2007. doi:10.1152/ajpcell.00221.2006.
46. **Kayser EB**, **Suthammarak W**, **Morgan PG**, **Sedensky MM.** Isoflurane selectively inhibits distal mitochondrial complex I in *Caenorhabditis elegans*. *Anesth Analg* 112: 1321–1329, 2011. doi:10.1213/ANE.0b013e3182121d37.
47. **Agarwal B**, **Dash RK**, **Stowe DF**, **Bosnjak ZJ**, **Camara AKS.** Isoflurane modulates cardiac mitochondrial bioenergetics by selectively attenuating respiratory complexes. *Biochim Biophys Acta* 1837: 354–365, 2014. doi:10.1016/j.bbabio.2013.11.006.
48. **Zimin PI**, **Woods CB**, **Kayser EB**, **Ramirez JM**, **Morgan PG**, **Sedensky MM.** Isoflurane disrupts excitatory neurotransmitter dynamics via inhibition of mitochondrial complex I. *Br J Anaesth* 120: 1019–1032, 2018. doi:10.1016/j.bja.2018.01.036.